Star Formation Newsletter No. 365 #25-36

Shota Notsu (Dept. of Astronomy, Univ. of Tokyo)

34. ALMA ACA study of the H₂S/OCS ratio in low-mass protostars

Tanya Kushwahaa, Maria N. Drozdovskaya, Łukasz Tychoniec, Benoît Tabone ★ The identification of the main sulfur reservoir on its way from the diffuse interstellar medium to the cold dense star-forming cores and eventually to protostars is a long-standing problem. Despite sulfur's astrochemical relevance, the abundance of S-bearing molecules in dense cores and regions around protostars is still insufficiently constrained. The goal of this investigation is to derive the gas-phase H_2S/OCS ratio for several low-mass protostars, which could provide crucial information about the physical and chemical conditions in the birth cloud of Sun-like stars. Using ALMA ACA Band 6 observations, H_2S, OCS, and their isotopologs are searched for in 10 Class 0/I protostars with different source properties such as age, mass, and environmental conditions. An LTE model is used to fit synthetic spectra to the detected lines and to derive the column densities based solely on optically thin lines. The H_2S and OCS column densities span four orders of magnitude across the sample. The H_2S/OCS ratio is found to be in the range from 0.2 to above 9.7. IRAS 16293-2422 A and Ser-SMM3 have the lowest ratio, while BHR71-IRS1 has the highest. Only the H_2S/OCS ratio of BHR71-IRS1 agress within uncertainties with the ratio in comet 67P/C−G. The determined gas-phase H_2S/OCS ratios can be below the upper limits on the solid-state ratios by as much as an order of magnitude. The H_2S/OCS ratio depends significantly on the environment of the birth cloud, such as UV-irradiation and heating received prior to the formation of a protostar. The highly isolated birth environment of BHR71-IRS1 is hypothesized to be the reason for its high gaseous H_2S/OCS ratio due to lower rates of photoreactions and more efficient hydrogenation reactions under such dark, cold conditions. The gaseous inventory of S-bearing molecules in BHR71-IRS1 appears to be most similar to that of interstellar ices.

ALMA ACAで(Band 6)、10個のClass 0/I原始星に対しH2SやOCSの観測を実施。
柱密度と共にH2S/OCS比を算出し、物理パラメータへの依存性や、S組成の進化史を議論

観測天体リスト

Table 2: Observed Class 0/I protostellar systems.

| Source	d (pc)	M_{env} ($M_\odot$)	L_{bol} ($L_\odot$)	T_{bol} (K)	Class –	v_{LSR} (km s^{-1})
IRAS 16293-2422 A	141[a]	4.0[d]	~18[b]	–	0	+3.2[c]
IRAS 16293-2422 B	141[a]	4.0[d]	~3[b]	–	0	+2.7[c]
NGC 1333-IRAS4A	299[e]	5.6[f]	9.1[f]	29[g]	0	+7.2[q]
RCrA IRS7B	130[i]	2.2[j]	4.6[j]	89[j]	0/I	+5.8[v]
Per-B1-c	301[e]	1.8[h]	3.84[h]	48[k]	0	+6.4[k]
BHR71-IRS1	200[o, p]	2.7[q]	15[q]	44[q]	0	-4.4[q]
Per-emb-25	294[r]	0.5[h]	1.0[h]	68[h]	0/I	+5.8[k]
NGC 1333-IRAS4B	299[e]	3.0[q]	4.4[q]	28[g]	0	+7.4[q]
Ser-SMM3	436[s]	3.2[q]	5.1[q]	38[q]	0	+7.6[q]
TMC1	140[t, u]	0.2[q]	0.9[q]	101[q]	I	+5.2[q]
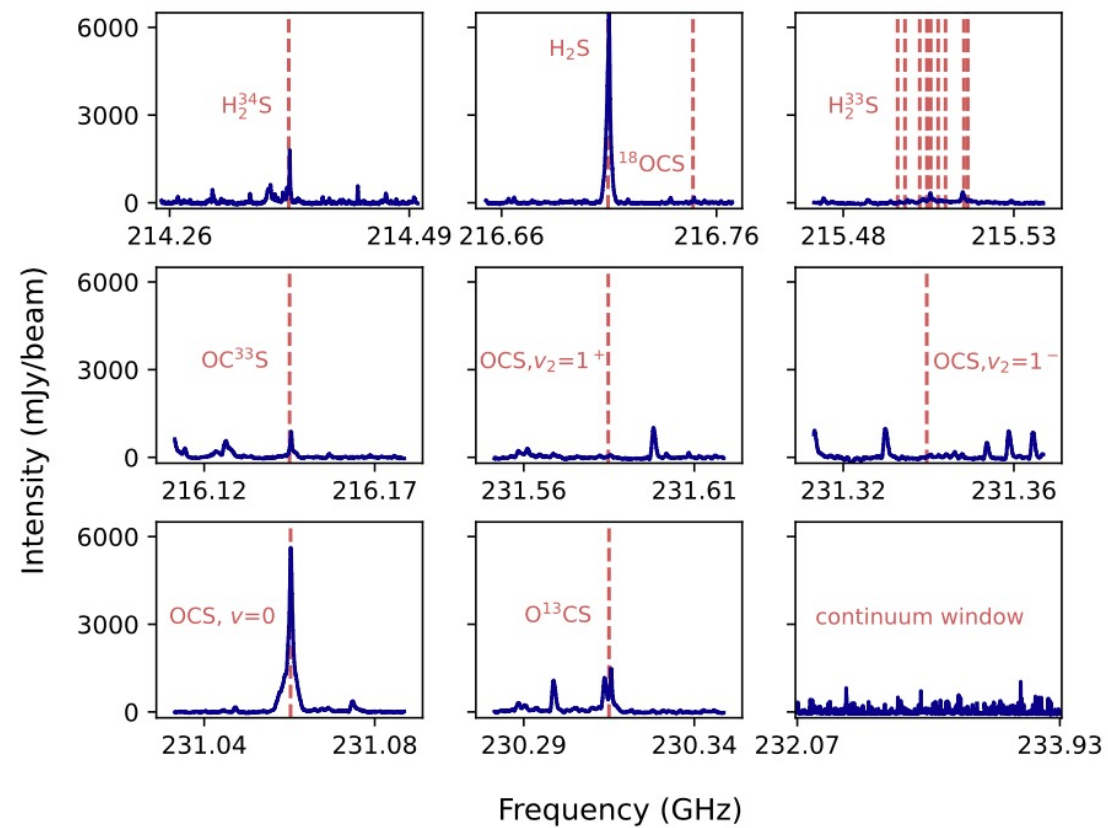
Figure 2: Observed spectral windows of IRAS 16293-2422 B (Table 3) obtained with ALMA ACA at Band 6 frequencies (Table 1). A Doppler shift by v_{LSR} = 2.7 km s^{-1} has been applied (Table 2).
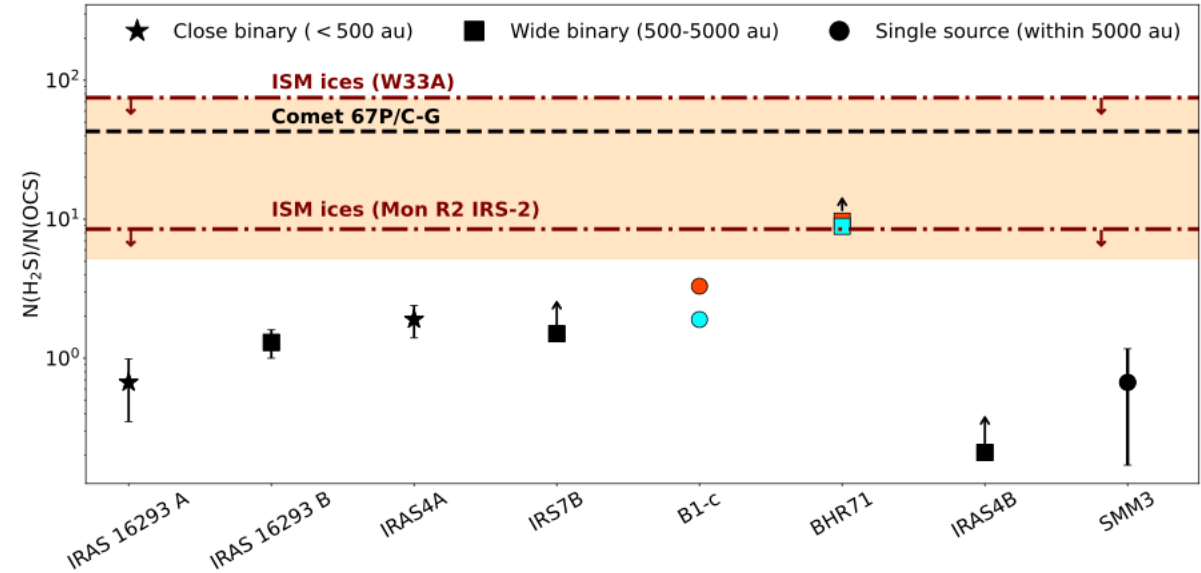
観測スペクトル
(IRAS16293-2422B)

観測で得られた柱密度 & H2S/OCS比

彗星やISM iceに比べ低いH2S/OCS比

Table 5: H₂S/OCS ratio for the studied sources, including their evolutionary class, binarity, environment, and the derived column densities of H₂S and OCS for the stated excitation temperatures. The H₂S/OCS ratios for the cold and warm components of B1-c, and the cold component of BHR71-IRS1 are the best-available estimates pending opacity issues.

Source	Class	Binarity	Environment	T_{ex} (K)	$N(H_2S)$ (cm^{-2})	$N(OCS)$ (cm^{-2})	$N(H_2S)/N(OCS)$
IRAS 16293-2422 A	0	CB	Clustered	125±20	(2.4±0.4)×10¹⁷	(3.6±1.4)×10¹⁷	0.7±0.3
IRAS 16293-2422 B	0	WB	Clustered	125±20	(9.2±1.7)×10¹⁶	(7.0±0.8)×10¹⁶	1.3±0.3
NGC 1333-IRAS4A	0	CB	Clustered	150-300	(3.4±0.8)×10¹⁶	(1.8±0.2)×10¹⁶	1.9±0.5
RCrA IRS7B	0/I	WB	Clustered	100±20	(5.6±0.8)×10¹³	≤3.6×10¹³	≥1.5
Per-B1-c	0	S	Clustered	60	>9.7×10¹⁵	>5.0×10¹⁵	(1.9)
				200	>1.2×10¹⁶	>3.6×10¹⁵	(3.3)
BHR71-IRS1	0	WB	Isolated	100	>2.4×10¹⁶	>2.7×10¹⁵	(8.9)
				250	>3.3×10¹⁶	(3.4±0.3)×10¹⁵	≥9.7
Per-emb-25	0/I	S	Clustered	50-300	≤8.3×10¹³	≤3.2×10¹⁴	–
NGC 1333-IRAS4B	0	WB	Clustered	100±20	>5.8×10¹⁵	(2.8±0.6)×10¹⁶	≥0.21
Ser-SMM3	0	S	Clustered	100-250	(5.8±3.2)×10¹⁴	(8.7±4.9)×10¹⁴	0.7±0.5
TMC1	I	CB	Clustered	40	≤1.5×10¹³	≤2.6×10¹³	–
Comet (67P/C-G)							$26.8^{+47.5,\,a}_{-21.6}$
					$N(H_2S)/N(H_2O)$	$N(OCS)/N(H_2O)$	$N(H_2S)/N(OCS)$
ISM ices (W33A)					<3.0×10⁻²,ᵇ	4.0×10⁻⁴,ᶜ	<75
ISM ices (Mon R2 IRS2)					<4.7×10⁻³,ᵈ	5.5×10⁻⁴,ᶜ	<8.5

Notes. CB: close binary (< 500 au) that is not spatially resolved in the data used for this work; WB: wide binary (500 − 5 000 au) that is spatially resolved in the data used for this work; S: single source within 5 000 au. ISM stands for interstellar medium. References: [a] Rubin et al. (2019), [b] van der Tak et al. (2003), [c] Palumbo et al. (1995), [d] Smith (1991).

多くの原始星(in clustered region)での低いH2S/OCS比
→光解離によるH2S→OCS反応が進んだ可能性
　& 温度が高くCO iceが少ないため、OCSがよりできやすい

BHR71-IRS1: 孤立した原始星なので反応が進みにくかった and/or
温度が低い為にCO iceが存在し、OCSへの反応が進みにくかった

星形成前のCloudの状態が化学進化に影響！

30. The Disc Miner II: Revealing Gas substructures and Kinematic signatures from Planet-disc interaction through line profile analysis

Andres F. Izquierdo, Leonardo Testi, Stefano Facchini, Giovanni P. Rosotti, Ewine van Dishoeck, Lisa Wölfer, Teresa Paneque-Carreño ★

[Abridged] The aim of this work is to identify potential signatures from planet-disc interaction in the circumstellar discs around MWC 480, HD 163296, AS 209, IM Lup, and GM Aur, through the study of molecular lines observed as part of the ALMA large program MAPS. Extended and localised perturbations in velocity, line width, and intensity have been analysed jointly using the DISCMINER modelling framework, in three bright CO lines, 12CO, 13CO, and C18O $J = 2 - 1$, to provide a comprehensive summary of the kinematic and column density substructures that planets might be actively sculpting in these discs. We find convincing evidence for the presence of four giant planets located at wide orbits in three of the discs in the sample: two around HD 163296, one in MWC 480, and one in AS 209. One of the planet candidates in HD 163296, P94, previously associated with velocity signatures detected in lower velocity resolution 12CO data, is confirmed and linked to localised velocity and line width perturbations in 13CO and C18O too. We highlight that line widths are also powerful tracers of planet-forming sites as they are sensitive to turbulent motions triggered by planet-disc interactions. In MWC 480, we identified non-axisymmetric line width enhancements around the radial separation of candidate planet-driven buoyancy spirals, which we used to narrow the location of the possible planet to an orbital radius of $R = 245$ au and PA = 193°. In the disc of AS 209, we found excess 12CO line widths centred at $R = 210$ au, PA = 151°, spanning around the immediate vicinity of a circumplanetary disc candidate proposed previously, which further supports its presence. Our simultaneous analysis of multiple tracers and observables aims to lay the groundwork for robust studies of molecular line properties focused on the search for young planets in discs.

ALMA Large Program MAPSで観測された5天体(MWC480, HD163296, AS209, IMLup, and GMAur)について、12CO, 13CO, C18O J=2-1輝線の速度プロファイルデータを再解析し、惑星-円盤相互作用に伴う速度擾乱などの存在を調査
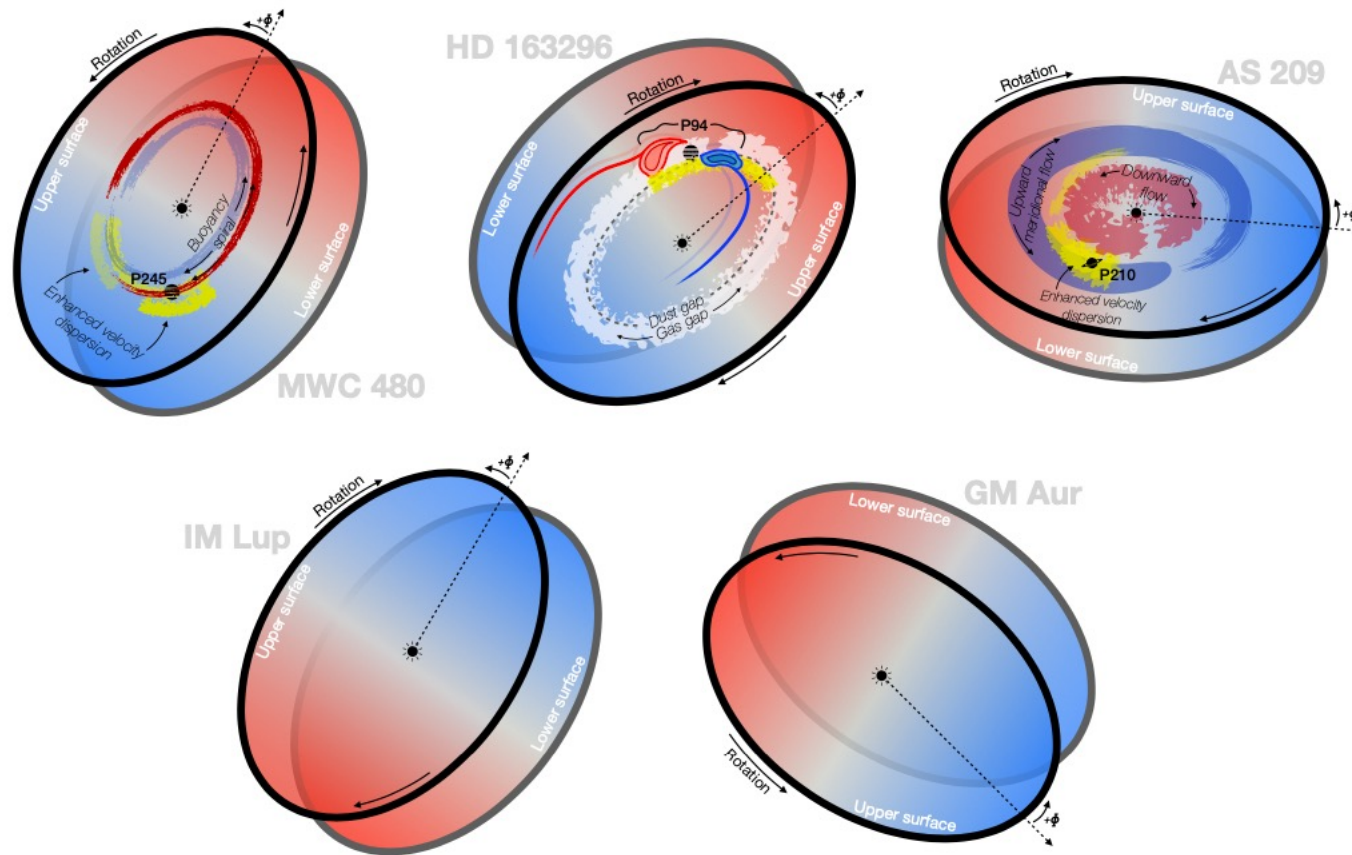
Fig. 1: Illustrating the orientation and rotation direction of the discs observed by the ALMA large program MAPS and analysed here. Dashed arrows mark the origin of each disc coordinate system. For convenience, we assume this reference axis to be parallel to the projected semi-major axis that is closest to the north celestial axis in counterclockwise rotation. Also shown are the signatures reported in this work as potential planet-disc interaction features in the form of both coherent and turbulent velocity fluctuations.

Table 1: List of attributes adopted in the DISCMINER models for this work.

Attribute	Prescription
Orientation	i, PA, x_c, y_c
Velocity	$v_{rot} = \sqrt{\frac{GM_*}{r^3}}R$, v_{sys}
Upper surface	$z_u = z_0(R/D_0)^p \exp\left[-(R/R_t)^q\right]$
Lower surface	$z_l = -z_0(R/D_0)^p \exp\left[-(R/R_t)^q\right]$
Peak intensity	$I_p = I_0(R/D_0)^p(z/D_0)^q$
Line width	$L_w = L_{w0}(R/D_0)^p(z/D_0)^q$
Line slope	$L_s = L_{s0}(R/D_0)^p$

Note. G is the gravitational constant; $D_0 = 100$ au is a normalisation factor. In disc coordinates, z is the height above the disc midplane, R is the cylindrical radius, and r is the spherical radius. The remaining variables are free parameters. All free parameters involved in each attribute are modelled independently, even if they are named alike.

観測天体の円盤と、発見された速度擾乱のまとめ

Table 2: Location of potential planet-driven signatures in discs reported in this and in previous works based on gas velocity perturbations and substructures, assuming that the planet candidate is in the disc midplane.

Planet	Location R [au]	φ [°]	R ["] PA [°]		Description of Signature	Reference / Data from [id]
HD 163296 c	94	50	0.77	352.1	Localised velocity perturbation in ^{12}CO	Izquierdo et al. (2022) / DSHARP [a]
	93	51	0.76	354.7	Localised velocity perturbation in ^{12}CO	This work (Fig. 6) / MAPS [b]
	83	–	–	–	Surface density gap traced by C^{18}O	Teague et al. (2018a) / Isella et al. (2016) [c]
	81	70	0.60	16.8	Localised velocity perturbation in ^{13}CO.	This work (Fig. 6) / MAPS
	79	74	0.58	22.0	Localised line width enhancement in ^{13}CO	This work (Fig. 8) / MAPS
	86	75	0.61	22.7	Localised line width enhancement in C^{18}O	This work (Fig. 8) / MAPS
	67–85	–	–	–	Extended line width enhancements in all COs	This work (Fig. 8) / MAPS
HD 163296 b	260	54*	2.20	357.0	Kink(s) in ^{12}CO intensity channels	Pinte et al. (2018a, 2020) / Isella et al. (2016) Calcino et al. (2022) / MAPS
	261	57	2.06	359.4	Localised velocity perturbation in ^{12}CO	Izquierdo et al. (2022) / DSHARP
	260–300	–	–	–	Extended velocity perturbation in ^{12}CO	Teague et al. (2021) / MAPS Izquierdo et al. (2022) / DSHARP
	250–320	–	–	–	Extended line width perturbations in ^{12}CO	This work (Fig. 8) / MAPS
MWC 480 b	245	–	–	–	Extended vertical flow, buoyancy spiral	Teague et al. (2021) / MAPS This work (Figs. 10, 13) / MAPS
	245	−128	1.33	192.6	Peak line width enhancement in ^{12}CO	This work (Fig. 10) / MAPS
AS 209 b	203*	−102*	1.40	161.0	Localised intensity feature in ^{13}CO	Bae et al. (2022b) / MAPS
	210	−110	1.44	151.3	Peak line width enhancement in ^{12}CO	This work (Fig. 11) / MAPS
	160–200	–	–	–	Extended high line widths in ^{12}CO and ^{13}CO	This work (Fig. 11) / MAPS
	200	−150, −60	–	–	Bending of iso-velocities in ^{12}CO	This work (Figs. 11, 12) / MAPS

Note. Radial locations and azimuths given in au and degrees, respectively, are referred to the disc reference frame. Radial separations and position angles given in arc-seconds and degrees are referred to the sky plane. The origin of sky coordinates is offset from the disc centre according to the model (x_c, y_c) values reported in tables A.1–A.5 for each disc. The disc orientation parameters used to convert coordinates from one reference system to the other are also summarised in said tables. *Value converted from sky coordinates reported in the referenced work to disc coordinates using orientation parameters retrieved in this work. *Project IDs* – [a](2016.1.00484.L; PI: S. Andrews). [b](2018.1.01055.L; PI: K. Öberg). [c](2013.1.00601.S; PI: A. Isella).
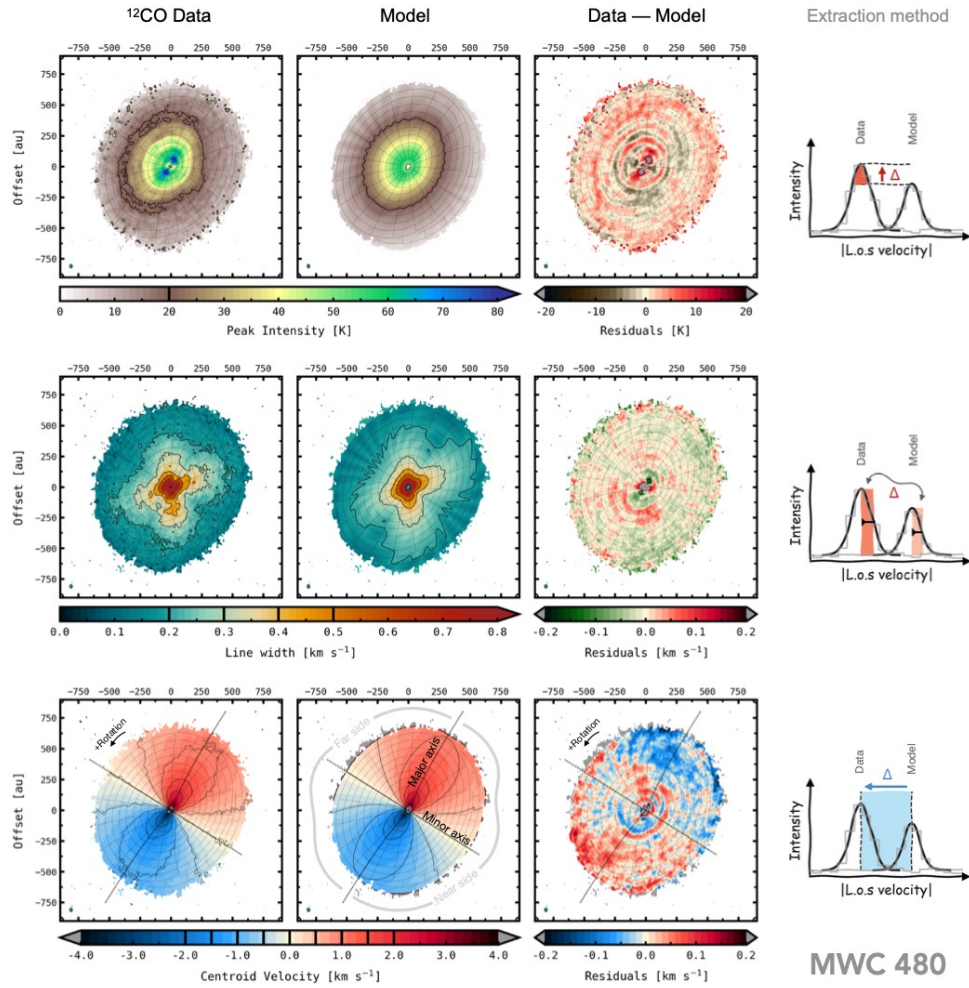
発見された擾乱構造のリスト

Fig. 3: Extraction of the line profile observables considered in this work, using MWC 480 ^{12}CO data as example. Peak intensities (top), line widths (middle), and centroid velocities (bottom) are displayed for both data and best-fit model, as well as residual maps showing the difference between them. Sketches on the rightmost column illustrate how each line profile observable is computed on the data cube and subsequently compared to those derived on the smooth, Keplerian model cube obtained by DISCMINER. The black solid lines are reference contours to ease comparison. Their levels are indicated in the colour bars. Residuals on each of the observables are driven by temperature, density and velocity fluctuations in the gas disc.
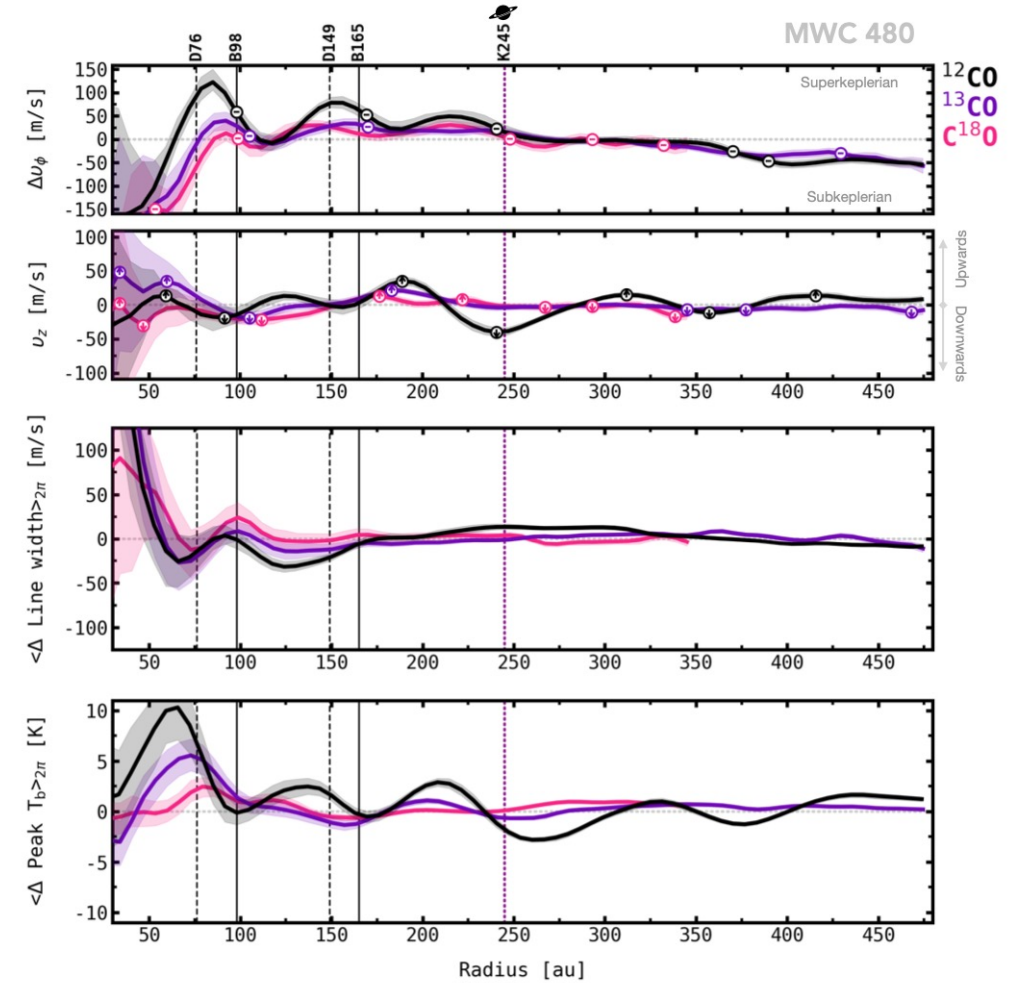
Fig. 13: Azimuthally averaged profiles of velocity (top), line width (middle) and peak intensity (bottom) residuals obtained for ^{12}CO, ^{13}CO, and C^{18}O, for the disc around MWC 480. The radial location of millimetre dust gaps and rings is illustrated as dashed and solid lines, respectively. The radial distance of the most prominent kink apparent in ^{12}CO channel maps is shown by the dotted purple line. Strong pressure bumps traced by minimal velocity gradients are marked with minuses in the top panel. Peak meridional flows hinting at gas moving away and towards the disc midplane are highlighted with arrows pointing up and down in the second top panel. The planet marker indicates the orbital radius of the planet candidate proposed at $R = 245$ au (see Table 2).
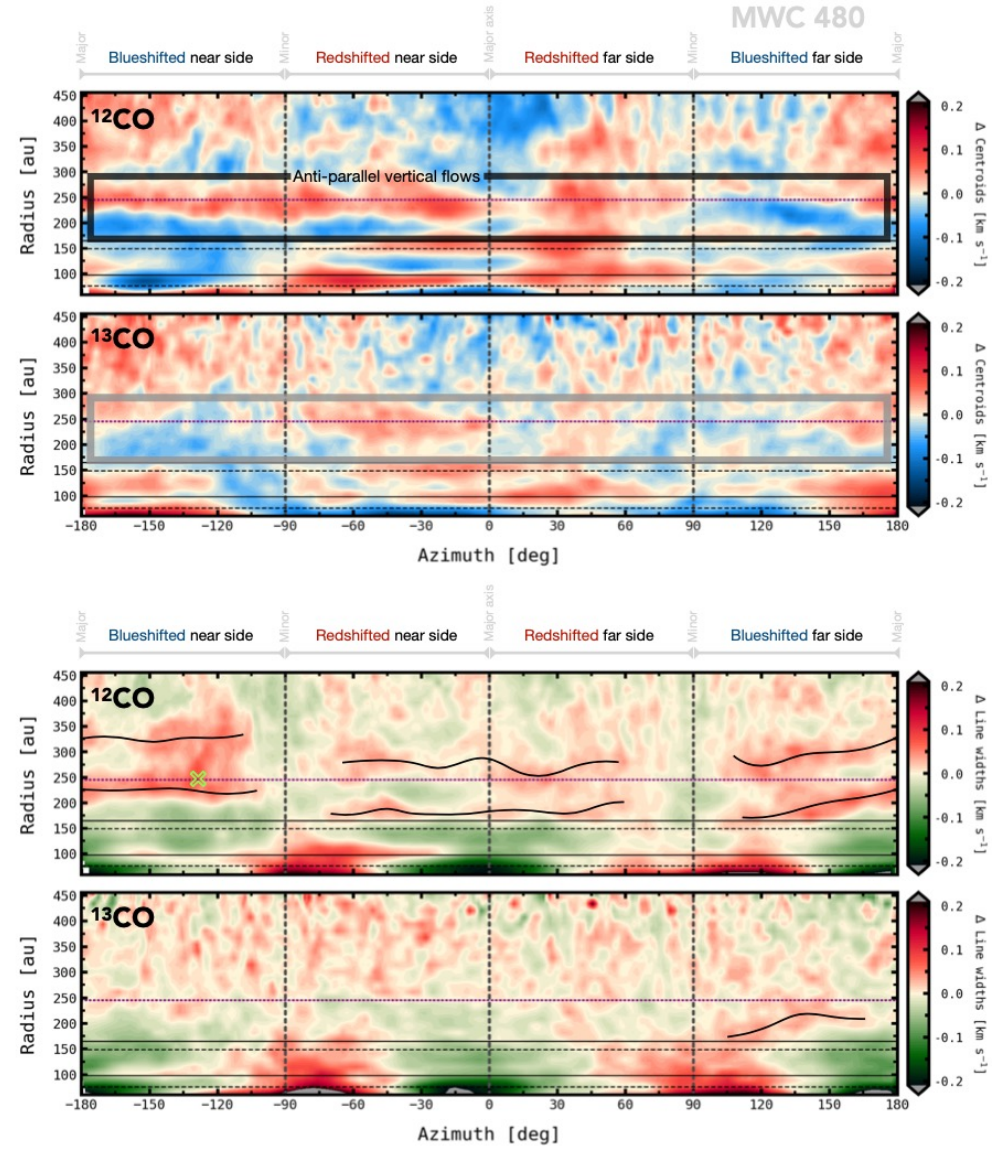
MWC480での解析例

Fig. 10: Azimuthal deprojection of velocity and line width residuals obtained for the disc of MWC 480 as observed in ^{12}CO and ^{13}CO. The horizontal dashed and solid lines indicate the radial location of dust gaps and rings, respectively. The purple dotted line is the radial location of kink-like features observed in the datacube channels. The vertical lines denote the azimuthal location of the disc main axes as projected on the sky. The black lines overlaid in the line width residuals highlight the location of extended line width enhancements, likely associated to non-thermal motions. The green cross marks the location of the planet candidate reported in Sect. 3.2 based on ^{12}CO line width enhancements. Cartesian versions of these maps can be found in Figs. 4 and B.7.

MWC480での解析例

27. Magnetic Activity-Rotation-Age-Mass Relations in Late Pre-main Sequence Stars

Konstantin V. Getman, Eric D. Feigelson, Gordon P. Garmire ★ We study the four-dimensional relationships between magnetic activity, rotation, mass and age for solar-type stars in the age range 5-25Myr. This is the late-pre-main sequence (l-PMS) evolutionary phase when rapid changes in star's interior may lead to the changes in magnetic dynamo mechanisms. We carefully derive rotational periods and spot sizes for 471 members of several l-PMS open clusters using photometric light curves from the Zwicky Transient Facility. Magnetic activity was measured in our previous Chandra-based study, and additional rotational data were obtained from other work. Several results emerge. Mass-dependent evolution of rotation through the l-PMS phase agrees with astrophysical models of stellar angular momentum changes, although the data point to a subpopulation of stars with slower initial rotations than commonly assumed. There is a hint of the onset of unsaturated tachoclinal dependency of X-ray activity on rotation, as reported by Argiroffi et al. (2016), but this result is not confidently confirmed. Both X-ray luminosity and star spot area decrease approximately as t^{-1} for solar mass stars suggesting that spot magnetic fields are roughly constant and l-PMS stars follow the universal solar-scaling law between the X-ray luminosity and surface magnetic flux. Assuming convective dynamos are dominant, theoretical magnetic fluxes fail to reveal the universal law for l-PMS stars that enter late Henyey tracks. Altogether we emerge with a few lines of evidence suggesting that the transition from the turbulent to solar-type dynamo occurs at the later stages of l-PMS evolution as stars approach the Zero-Age Main Sequence.

年齢5-25Myrの後期前主系列星の磁気活動性の回転・年齢等に対する依存性を調べた
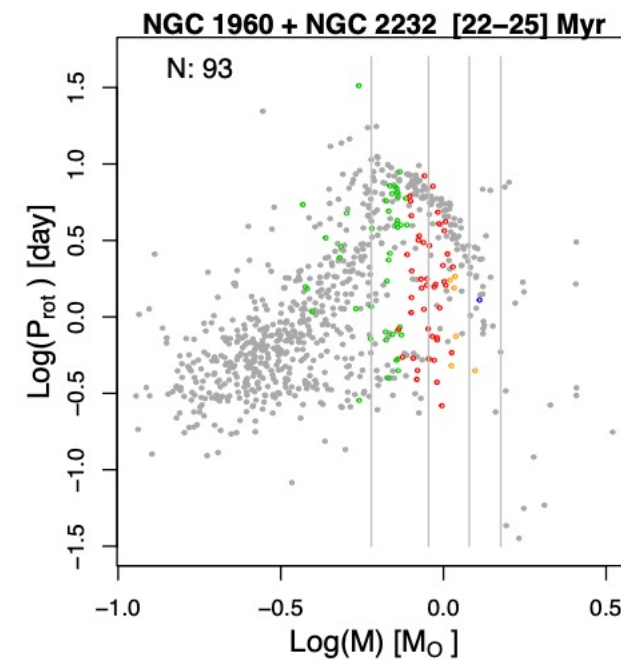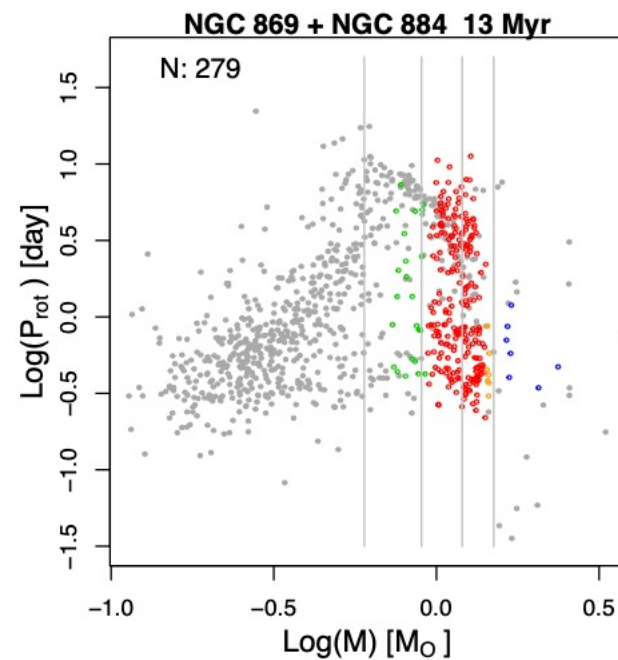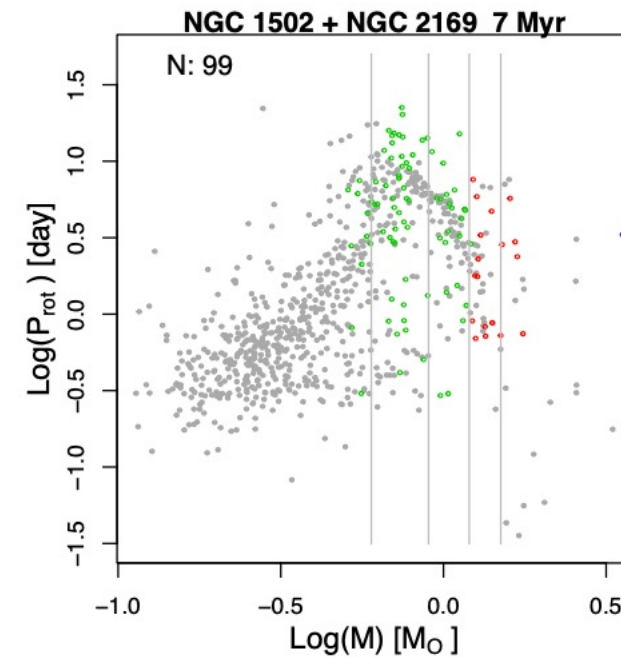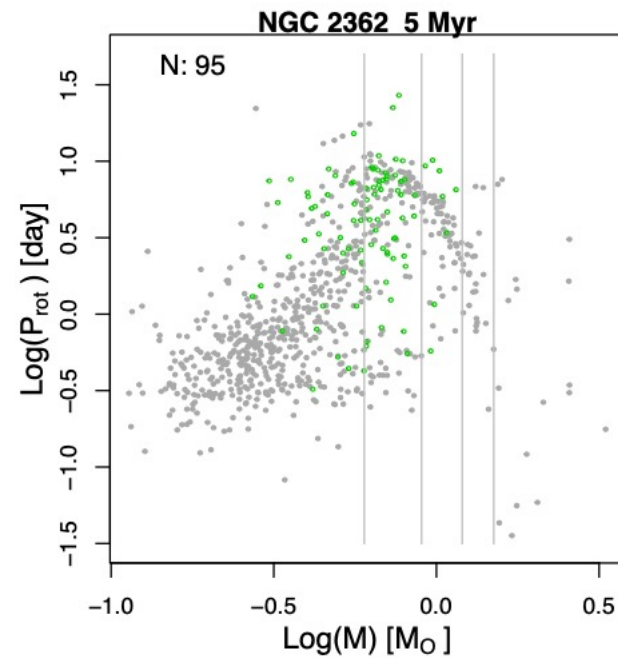Zwicky Transient Facility (ZTF) Surveyの可視光光度曲線データのほか、ChandraのX線データなども使用
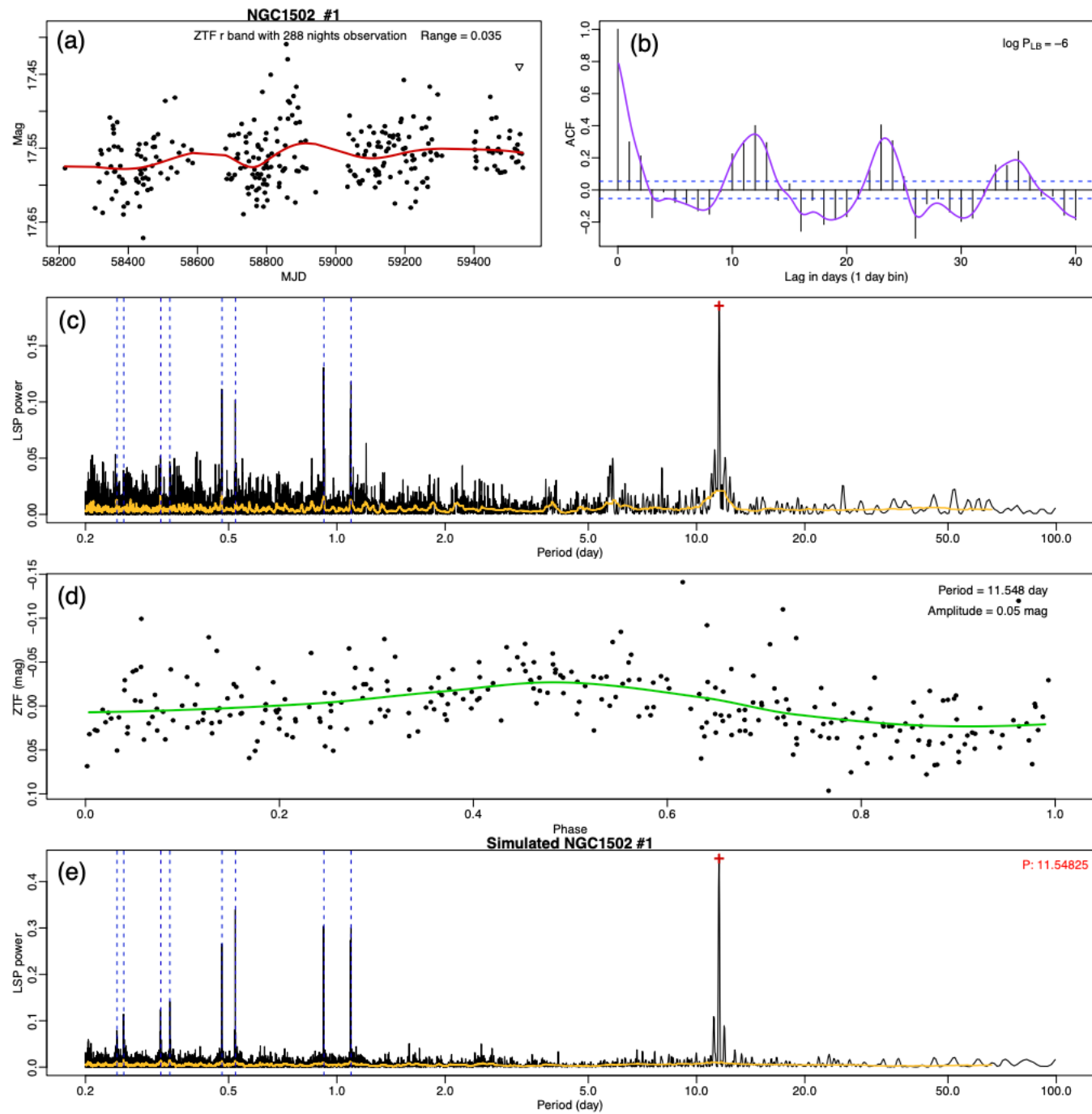
ZTF Surveyの観測データ
と、周期解析の例

周期 vs 星質量関係
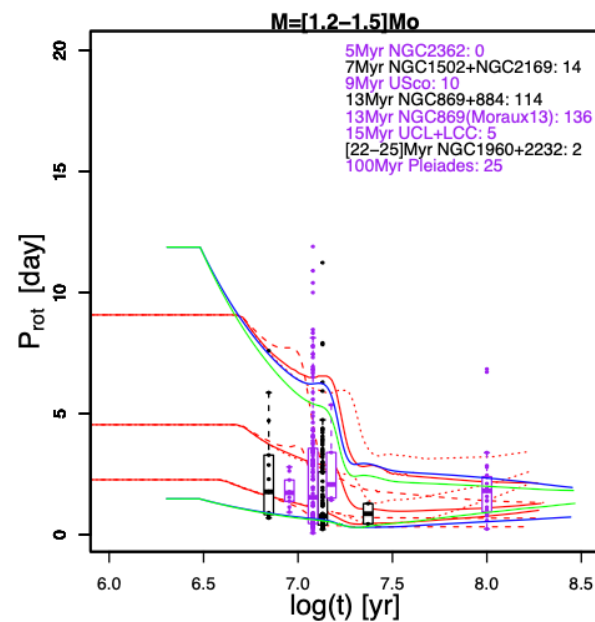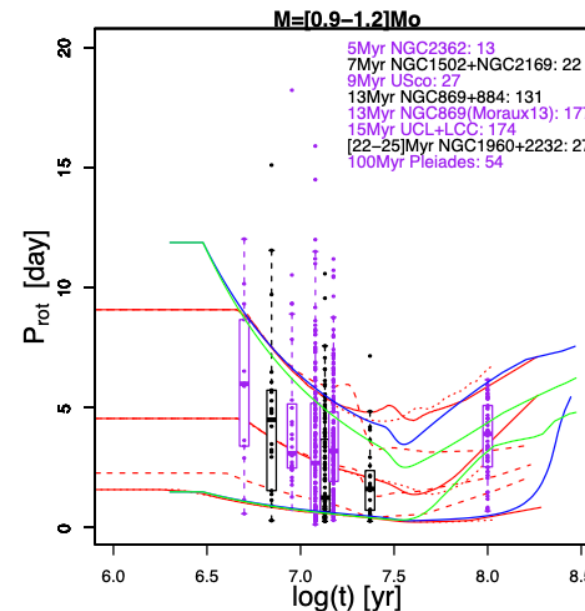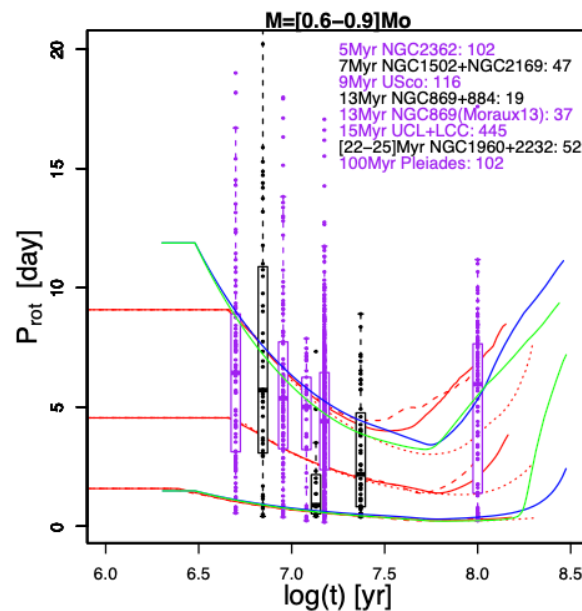
緑色：Hayashi track
赤色：early Henyey track
オレンジ色：late Henyey track
青色：ZAMS-MS
の星

灰色：プレアデス星団の星
（比較のためplot）

年齢 vs 星自転速度

観測データと
モデル計算の比較図

M=[0.6-0.9]Mo

5Myr NGC2362: 102
7Myr NGC1502+NGC2169: 47
9Myr USco: 116
13Myr NGC869+884: 19
13Myr NGC869(Moraux13): 37
15Myr UCL+LCC: 445
[22-25]Myr NGC1960+2232: 52
100Myr Pleiades: 102

M=[0.9-1.2]Mo

5Myr NGC2362: 13
7Myr NGC1502+NGC2169: 22
9Myr USco: 27
13Myr NGC869+884: 131
13Myr NGC869(Moraux13): 177
15Myr UCL+LCC: 174
[22-25]Myr NGC1960+2232: 27
100Myr Pleiades: 54

M=[1.2-1.5]Mo

5Myr NGC2362: 0
7Myr NGC1502+NGC2169: 14
9Myr USco: 10
13Myr NGC869+884: 114
13Myr NGC869(Moraux13): 136
15Myr UCL+LCC: 5
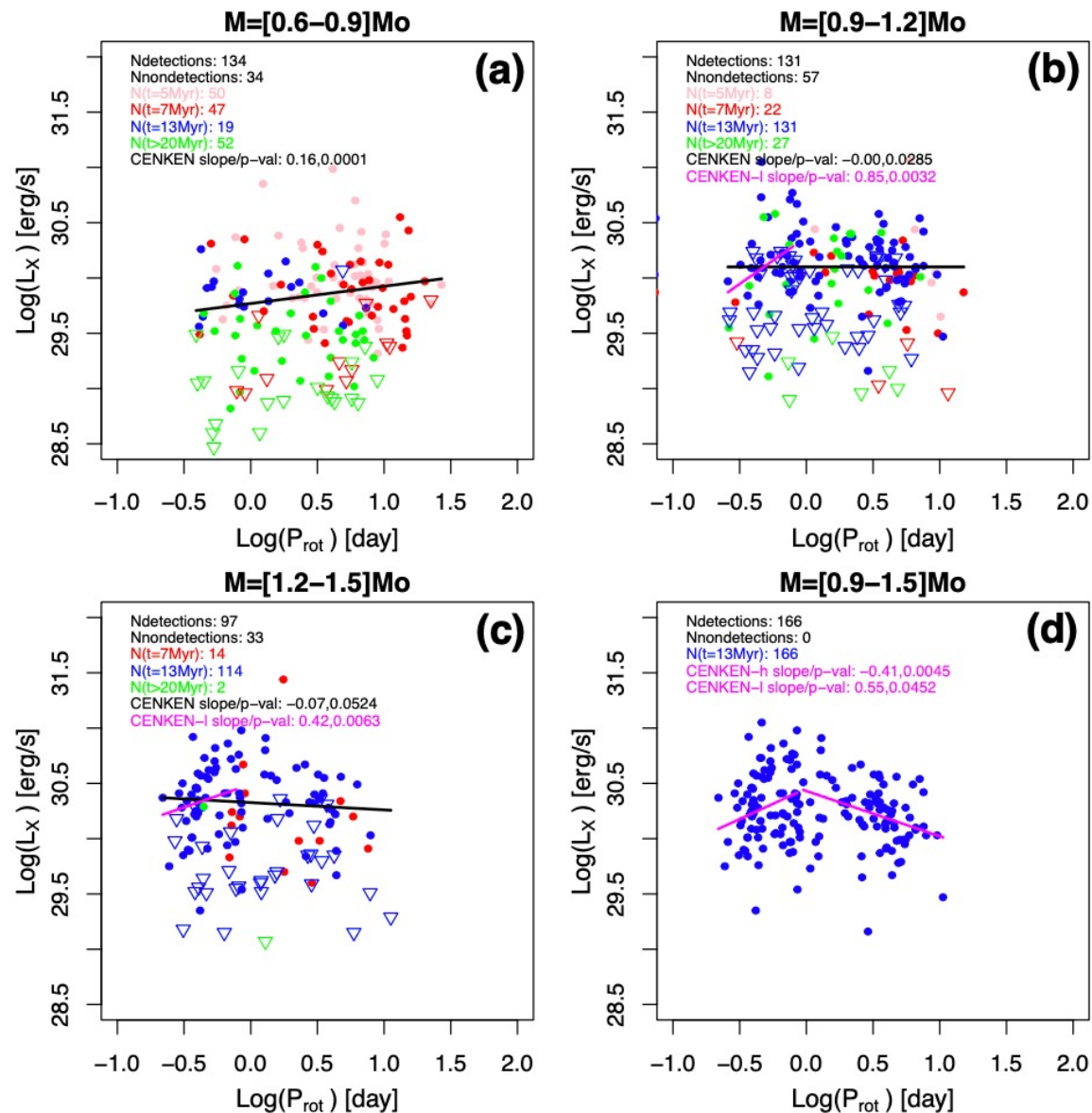[22-25]Myr NGC1960+2232: 2
100Myr Pleiades: 25

自転周期 vs X線光度

Figure 6. X-ray luminosity as a function of rotation period for the l-PMS stars in Table 1. Panels (a,b,c) show $L_X - P_{rot}$ distributions for different mass strata. X-ray detections (circles) and X-ray non-detections (triangles) are color-coded according to stellar age: 5 Myr (pink), 7 Myr (red), 13 Myr (blue), and > 20 Myr (green). Black and magenta lines are calculated using the Akritas-Thiel-Sen statistical procedure; see text for detail. Panel (d) shows $L_X - P_{rot}$ distribution for 13 Myr old stars that were detected in X-rays in the $0.9 - 1.5$ M$_\odot$ range.
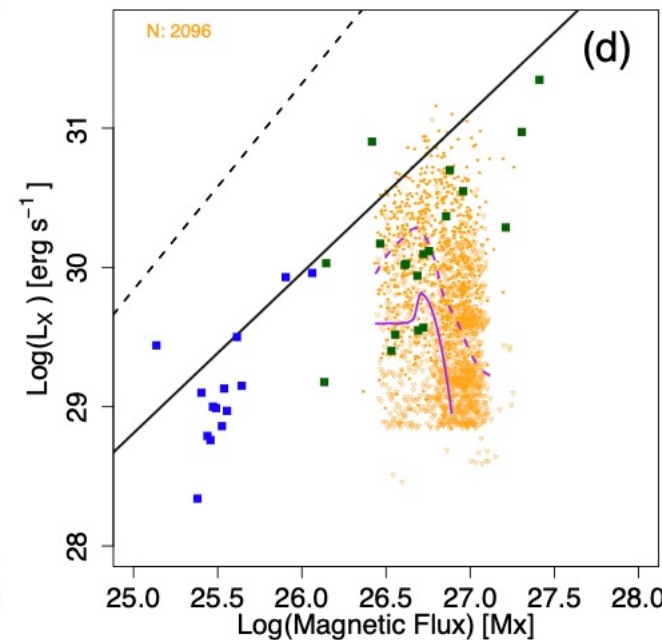
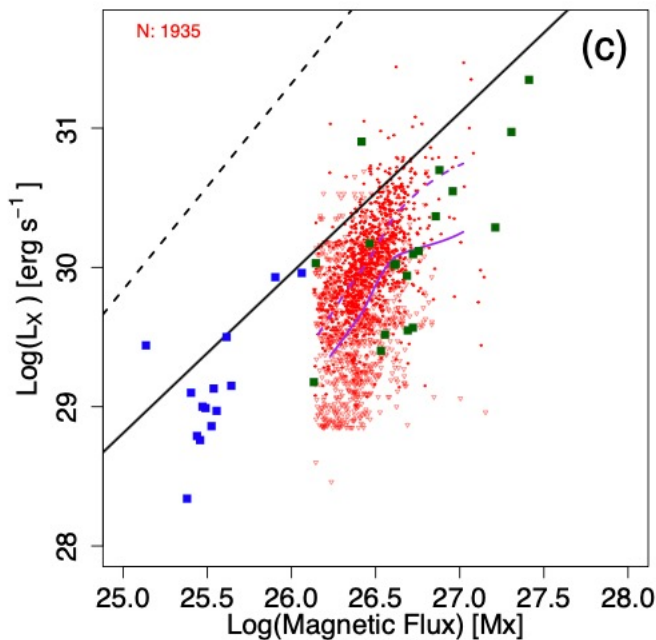Magnetic Flux vs X線光度
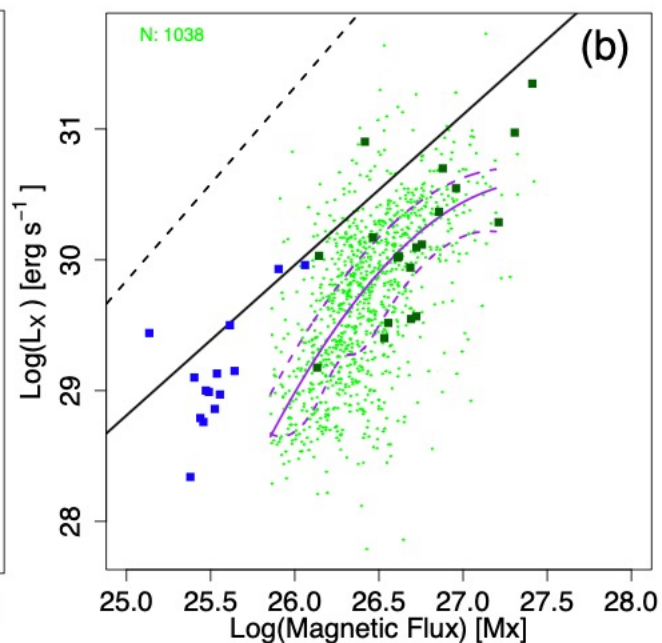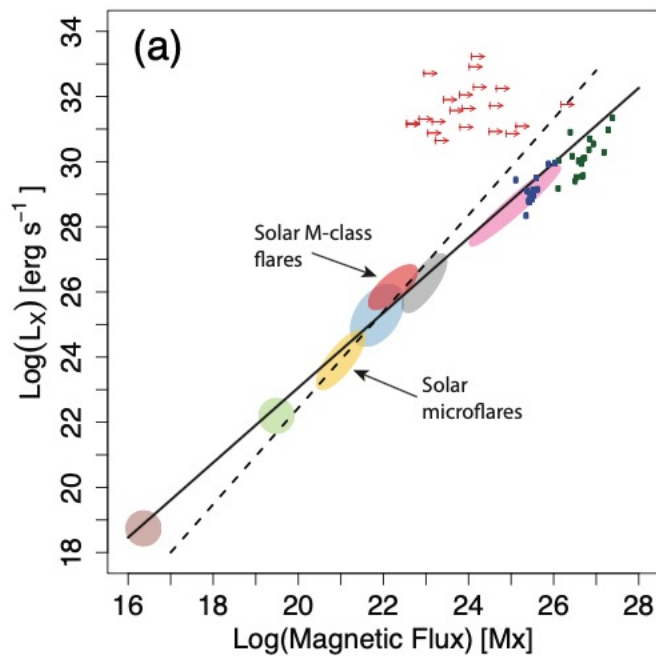
緑色：Hayashi track
赤色：early Henyey track
オレンジ色：late Henyey track &ZAMS-MS
の星

緑点：先行研究の前主系列星のデータ

Magnetic Fluxは光度変動幅→黒点サイズから算出

Plot dのみずれがある
→全球対流からsolor system dynamoへの変化を
示唆?

32.

A 3D physico-chemical model of a pre-stellar core. I. Environmental and structural impact on the distribution of CH_3OH and c-C_3H_2

S. S. Jensen, S. Spezzano, P. Caselli, T. Grassi, T. Haugbølle ★ Pre-stellar cores represent the earliest stage of the star- and planet-formation process. By characterizing the physical and chemical structure of these cores we can establish the initial conditions for star and planet formation and determine to what degree the chemical composition of pre-stellar cores is inherited to the later stages. A 3D MHD model of a pre-stellar core embedded in a dynamic star-forming cloud is post-processed using sequentially continuum radiative transfer, a gas-grain chemical model, and a line-radiative transfer model. Results are analyzed and compared to observations of CH_3OH and c-C_3H_2 in L1544. Nine different chemical models are compared to the observations to determine which initial conditions are compatible with the observed chemical segregation in the prototypical pre-stellar core L1544. The model is able to reproduce several aspects of the observed chemical differentiation in L1544. Extended methanol emission is shifted towards colder and more shielded regions of the core envelope while c-C_3H_2 emission overlaps with the dust continuum, consistent with the observed chemical structure. Increasing the strength of the interstellar radiation field or the cosmic-ray ionization rate with respect to the typical values assumed in nearby star-forming regions leads to synthetic maps that are inconsistent with the observed chemical structure. Our model shows that the observed chemical dichotomy in L1544 can arise as a result of uneven illumination due to the asymmetrical structure of the 3D core and the environment within which the core has formed. This highlights the importance of the 3D structure at the core-cloud transition on the chemistry of pre-stellar cores.

Pre-stellar coreの3D 物理(MHD)-化学モデル計算を実施
L1544のc-C3H2とCH3OHの分布の再現を目指す
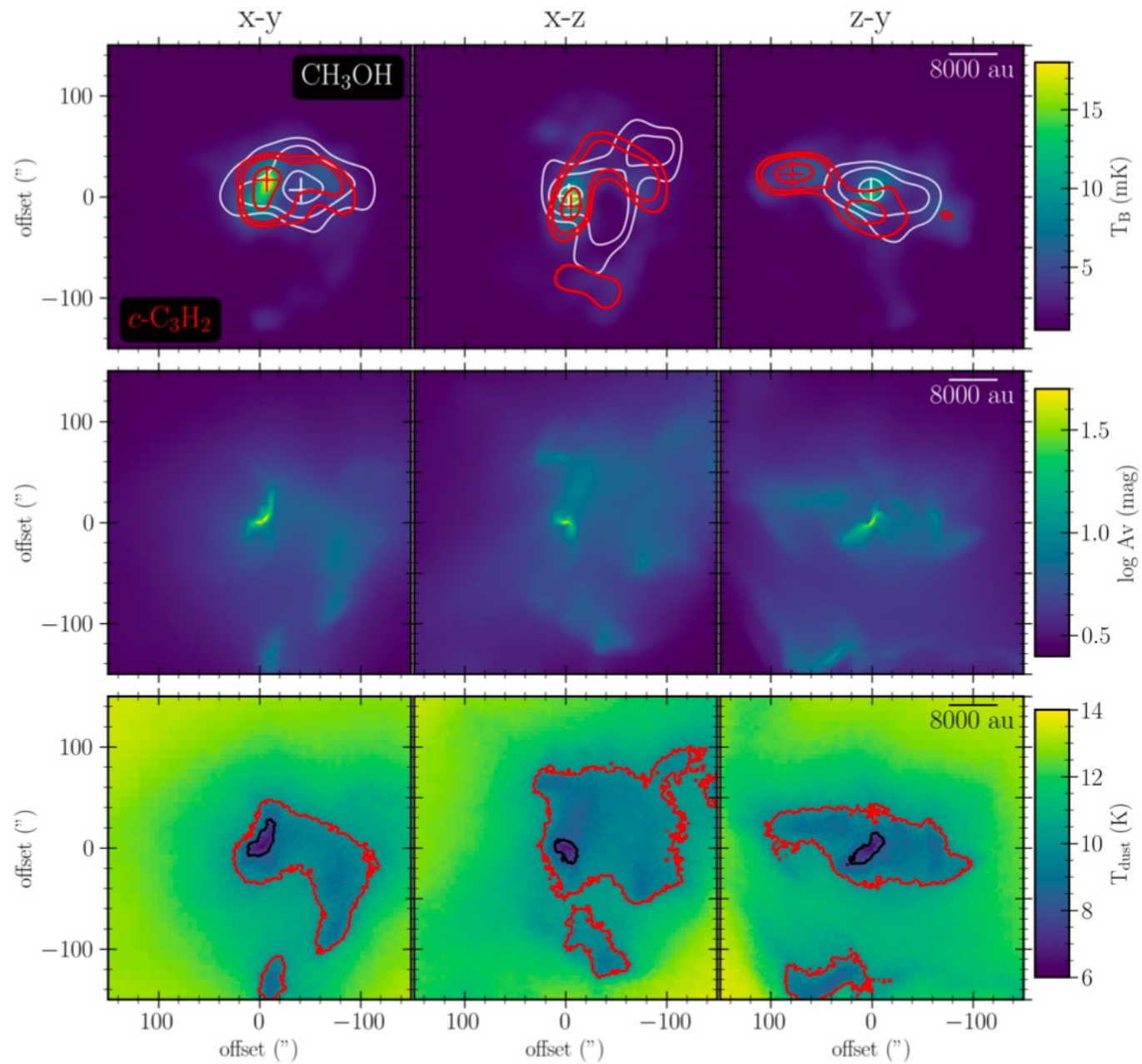
25. The origin of dust polarization in the Orion Bar

Valentin J. M. Le Gouellec, B-G Andersson, Archana Soam, Thiébaut Schirmer, Joseph M. Michail, Enrique Lopez-Rodriguez, Sophia Flores, David T. Chuss, John E. Vaillancourt, Thiem Hoang, Alex Lazarian ★ The linear polarization of thermal dust emission provides a powerful tool to probe interstellar and circumstellar magnetic fields, because aspherical grains tend to align themselves with magnetic field lines. While the Radiative Alignment Torque (RAT) mechanism provides a theoretical framework to this phenomenon, some aspects of this alignment mechanism still need to be quantitatively tested. One such aspect is the possibility that the reference alignment direction changes from the magnetic field ("B-RAT") to the radiation field k-vector ("k-RAT") in areas of strong radiation fields. We investigate this transition toward the Orion Bar PDR, using multi-wavelength SOFIA HAWC+ dust polarization observations. The polarization angle maps show that the radiation field direction is on average not the preferred grain alignment axis. We constrain the grain sizes for which the transition from B-RAT to k-RAT occur in the Orion Bar (grains > 0.1 μm toward the most irradiated locations), and explore the radiatively driven rotational disruption that may take place in the high-radiation environment of the Bar for large grains. While the grains susceptible to rotational disruption should be in supra-thermal rotation and aligned with the magnetic field, k-RAT aligned grains would rotate at thermal velocities. We find that the grain size at which the alignment shifts from B-RAT to k-RAT corresponds to grains too large to survive the rotational disruption. Therefore, we expect a large fraction of grains to be aligned at supra-thermal rotation with the magnetic field, and potentially be subject to rotational disruption depending on their tensile strength.

26. Large-scale Velocity-coherent Filaments in the SEDIGISM Survey: Association with Spiral Arms and Fraction of Dense Gas

Y. Ge, K. Wang, A. Duarte-Cabral, A. R. Pettitt, C. L. Dobbs, Á. Sánchez-Monge, K. R. Neralwar, J. S. Urquhart, D. Colombo, E. Durán-Camacho, H. Beuther, L. Bronfman, A. J. Rigby, D. Eden, S. Neupane, P. Barnes, T. Henning, A. Y. Yang ★

Context. Filamentary structures in the interstellar medium are closely related to star formation. Dense gas mass fraction (DGMF) or clump formation efficiency in large-scale filaments possibly determine their hosting star formation activities. Aims. We aim to automatically identify large-scale filaments, characterize them, investigate their association with Galactic structures, and study their DGMFs. Methods. We use a modified minimum spanning tree (MST) algorithm to chain parsec-scale 13CO clumps previously extracted from the SEDIGISM (Structure, Excitation, and Dynamics of the Inner Galactic InterStellar Medium) survey. The MST connects nodes in a graph such that the sum of edge lengths is minimum. Modified MST also ensures velocity coherence between nodes, so the identified filaments are coherent in position-position-velocity (PPV) space. Results. We generate a catalog of 88 large-scale ($> 10pc$) filaments in the inner Galactic plane (with $-60° < l < 18°$ and $|b| < 0.5°$). These SEDIGISM filaments are larger and less dense than MST filaments previously identified from the BGPS and ATLASGAL surveys. We find that eight of the filaments run along spiral arms and can be regarded as "bones" of the Milky Way. We also find three bones associated with the Local Spur in PPV space. By compiling 168 large-scale filaments with available DGMF across the Galaxy, an order of magnitude more than previously investigated, we find that DGMFs do not correlate with Galactic location, but bones have higher DGMFs than other filaments.

28. ## A deep optical survey of young stars in the Carina Nebula. I. – UBVRI photometric data and fundamental parameters

Hyeonoh Hur, Beomdu Lim, Moo-Young Chun ★ We present the deep homogeneous $UBVRI$ photometric data of 135,071 stars down to $V \sim 23$ mag and I 22 mag toward the Carina Nebula. These stars are cross-matched with those from the previous surveys in the X-ray, near-infrared, and mid-infrared wavelengths as well as the Gaia Early Data Release 3 (EDR3). This master catalog allows us to select reliable members and determine the fundamental parameters distance, size, stellar density of stellar clusters in this star-forming region. We revisit the reddening toward the nebula using the optical and the near-infrared colors of early-type stars. The foreground reddening $[E(B\text{-}V)_{fg}]$ is determined to be 0.35+/-0.02, and it seems to follow the standard reddening law. On the other hand, the total-to-selective extinction ratio of the intracluster medium (R_V,cl) decreases from the central region (Trumpler 14 and 16, R_V,cl 4.5) to the northern region (Trumpler 15, R_V,cl 3.4). It implies that the central region is more dusty than the northern region. We find that the distance modulus of the Carina Nebula to be 11.9+/-0.3 mag (d = 2.4+/-0.35 kpc) using a zero-age main-sequence fitting method, which is in good agreement with that derived from the Gaia EDR3 parallaxes. We also present the catalog of 3,331 pre-main-sequence (PMS) members and 14,974 PMS candidates down to V 22 mag based on spectrophotometric properties of young stars at infrared, optical, and X-ray wavelengths. From the spatial distribution of PMS members and PMS candidates, we confirm that the member selection is very reliable down to faint stars. Our data will have a legacy value for follow-up studies with different scientific purposes.

29. **Unveiling the initial conditions of open star cluster formation**

C. J. Hao, Y. Xu, L. G. Hou, Z. H. Lin, Y. J. Li ★ Open clusters (OCs) are infrequent survivors of embedded clusters gestated in molecular clouds. Up to now, little is known about the initial conditions for the formation of OCs. Here, we studied this issue using high-precision astrometric parameters provided by Gaia data release 3. The statistics show that the peculiar motion velocities of OCs vary little from infancy to old age, providing a remarkable opportunity to use OCs to trace their progenitors. Adopting a dynamical method, we derived the masses of the progenitor clumps where OCs were born, which have statistical characteristics comparable to previously known results for clumps observed in the Galaxy. Moreover, the masses of the progenitor clumps of OCs indicate they should be capable of gestating massive O-type stars. In fact, after inspecting the observed OCs and O-type stars, we found that there are many O-type stars in OCs. The destructive stellar feedback from O-type stars may disintegrate the vast majority of embedded clusters, and only those sufficiently dense ones can survive as OCs.

31.
Study of the long-term BVR_cI_c photometric variability of eight PMS stars in the young open cluster Trumpler 37

Sunay Ibryamov, Gabriela Zidarova, Evgeni Semkov, Stoyanka Peneva ★
This paper reports results from our long-term $BV(RI)_c$ photometric CCD observations of eight pre-main-sequence stars collected from June 2008 to October 2022. These stars are located in the young open cluster Trumpler 37, in the field of GM Cephei. The observational data indicate that all stars from our study exhibit variability in all-optical passbands, typical for young stars. In this paper, we describe and discuss the photometric behavior of the stars and the possible reasons for their variability. For two of the objects, we identified periodicity in their light variation.

33.

FacetClumps: A Facet-based Molecular Clump Detection Algorithm

Yu Jiang, Zhiwei Chen, Sheng Zheng, Zhibo Jiang, Yao Huang, Shuguang Zeng, Xiangyun Zeng, Xiaoyu Luo

★ A comprehensive understanding of molecular clumps is essential for investigating star formation. We present an algorithm for molecular clump detection, called FacetClumps. This algorithm uses a morphological approach to extract signal regions from the original data. The Gaussian Facet model is employed to fit the signal regions, which enhances the resistance to noise and the stability of the algorithm in diverse overlapping areas. The introduction of the extremum determination theorem of multivariate functions offers theoretical guidance for automatically locating clump centers. To guarantee that each clump is continuous, the signal regions are segmented into local regions based on gradient, and then the local regions are clustered into the clump centers based on connectivity and minimum distance to identify the regional information of each clump. Experiments conducted with both simulated and synthetic data demonstrate that FacetClumps exhibits great recall and precision rates, small location error and flux loss, a high consistency between the region of detected clump and that of simulated clump, and is generally stable in various environments. Notably, the recall rate of FacetClumps in the synthetic data, which comprises ^{13}CO $(J = 1 - 0)$ emission line of the MWISP within $11.7° \leq l \leq 13.4°$, $0.22° \leq b \leq 1.05°$ and 5 km s$^{-1} \leq v \leq 35$ km s^{-1} and simulated clumps, reaches 90.2%. Additionally, FacetClumps demonstrates satisfactory performance when applied to observational data.

35. The interplay between pebble and planetesimal accretion in population synthesis models and its role in giant planet formation

Andrin Kessler, Yann Alibert ★ In the core accretion scenario of planet formation, rocky cores grow by first accreting solids until they are massive enough to accrete gas. For giant planet formation this means that a massive core must form within the lifetime of the gas disk. The accretion of roughly km-sized planetesimals and the accretion of mm-cm sized pebbles are typically discussed separately as the main solid accretion mechanisms. We investigate the interplay between the two accretion processes in a disk containing both pebbles and planetesimals for planet formation in general and in the context of giant planet formation specifically. The goal is to disentangle and understand the fundamental interactions that arise in such hybrid pebble-planetesimal models. We combine a simple model of pebble formation and accretion with a global model of planet formation which considers the accretion of planetesimals. We compare synthetic populations of planets formed in disks composed of different amounts of pebbles and 600 meter sized planetesimals. On a system-level, we study the formation pathway of giant planets in these disks. We find that, in hybrid disks containing both pebbles and planetesimals, the formation of giant planets is strongly suppressed whereas in a pebbles-only or planetesimals-only scenario, giant planets can form. We identify the heating associated with the accretion of up to 100 km sized planetesimals after the pebble accretion period to delay the runaway gas accretion of massive cores. Coupled with strong inward type-I migration acting on these planets, this results in close-in icy sub-Neptunes originating from the outer disk. We conclude that, in hybrid pebble-planetesimal scenarios, the late accretion of planetesimals is a critical factor in the giant planet formation process and that inward migration is more efficient for planets in increasingly pebble dominated disks.

36. Impact of turbulence intensity and fragmentation velocity on dust particle size evolution and non-ideal magnetohydrodynamics effects

Yoshihiro Kawasaki, Masahiro N. Machida ★
We investigate the influence of dust particle size evolution on non-ideal magnetohydrodynamic effects during the collapsing phase of star-forming cores, taking both the turbulence intensity in the collapsing cloud core and the fragmentation velocity of dust particles as parameters. When the turbulence intensity is small, the dust particles do not grow significantly, and the non-ideal MHD effects work efficiently in high-density regions. The dust particles rapidly grow in a strongly turbulent environment, while the efficiency of non-ideal MHD effects in such an environment depends on the fragmentation velocity of the dust particles. When the fragmentation velocity is small, turbulence promotes coagulation growth and collisional fragmentation of dust particles, producing small dust particles. In this case, the adsorption of charged particles on the dust particle surfaces becomes efficient and the abundance of charged particles decreases, making non-ideal MHD effects effective at high densities. On the other hand, when the fragmentation velocity is high, dust particles are less likely to fragment, even if the turbulence is strong. In this case, the production of small dust particles become inefficient and non-ideal MHD effects become less effective. We also investigate the effect of the dust composition on the star and disk formation processes. We constrain the turbulence intensity of a collapsing core and the fragmentation velocity of dust for circumstellar disk formation due to the dissipation of the magnetic field.